Titre: Title:	Single pulse nanosecond laser-stimulated targeted delivery of anti-cancer drugs from hybrid lipid nanoparticles containing 5 nm gold nanoparticles. Supplément
Auteurs: Authors:	Antoine Uzel, Leonidas Agiotis, Amélie Baron, Igor V. Zhigaltsev, Pieter R. Cullis, Morteza Hasanzadeh Kafshgari, & Michel Meunier
Date:	2023
Type:	Article de revue / Article
Référence: Citation:	Uzel, A., Agiotis, L., Baron, A., Zhigaltsev, I. V., Cullis, P. R., Kafshgari, M. H., & Meunier, M. (2023). Single pulse nanosecond laser-stimulated targeted delivery of anti-cancer drugs from hybrid lipid nanoparticles containing 5 nm gold nanoparticles. Small, 19(52), 2305591 (11 pages). https://doi.org/10.1002/smll.202305591

NANO · MICRO small

Supporting Information

for *Small*, DOI 10.1002/smll.202305591

Single Pulse Nanosecond Laser-Stimulated Targeted Delivery of Anti-Cancer Drugs from Hybrid Lipid Nanoparticles Containing 5 nm Gold Nanoparticles

Antoine Uzel, Leonidas Agiotis, Amélie Baron, Igor V. Zhigaltsev, Pieter R. Cullis, Morteza Hasanzadeh Kafshgari and Michel Meunier**

Supporting Information

Single pulse nanosecond laser-stimulated targeted delivery of anti-cancer drugs from hybrid lipid nanoparticles containing 5 nm gold nanoparticles

Antoine Uzel,[1] Leonidas Agiotis,[1] Amélie Baron,[1] Igor.V. Zhigaltsev,[2] Pieter R. Cullis,[2] Morteza Hasanzadeh Kafshgari[1,*] and Michel Meunier[1,*]

[1] Department of Engineering Physics, Polytechnique Montréal, Montreal, QC H3C 3A7, Canada
[2] Department of Biochemistry and Molecular Biology, University of British Columbia, 2350 Health Sciences Mall, Vancouver, BC V6T 1Z3, Canada

S.1. Stimuli-responsive intracellular DOX release

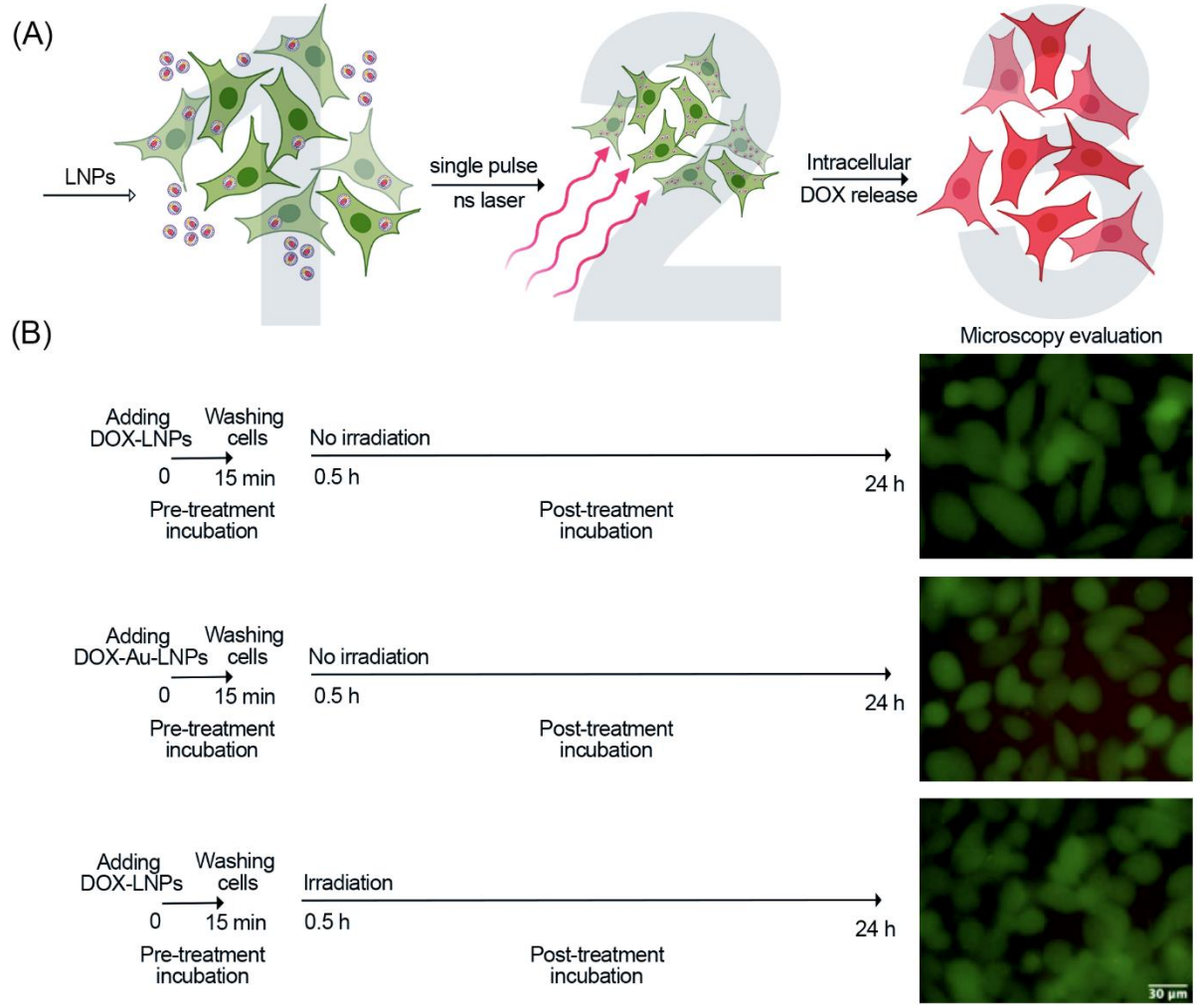

Figure S1. (A) Representative schematic of stimuli-responsive intracellular DOX release following strategy-I (15 min pre-incubation with LNPs). (B) Different control groups of DOX-Au-LNPs (50 µg/mL) and DOX-LNPs (50 µg/mL) with and without the irradiation.

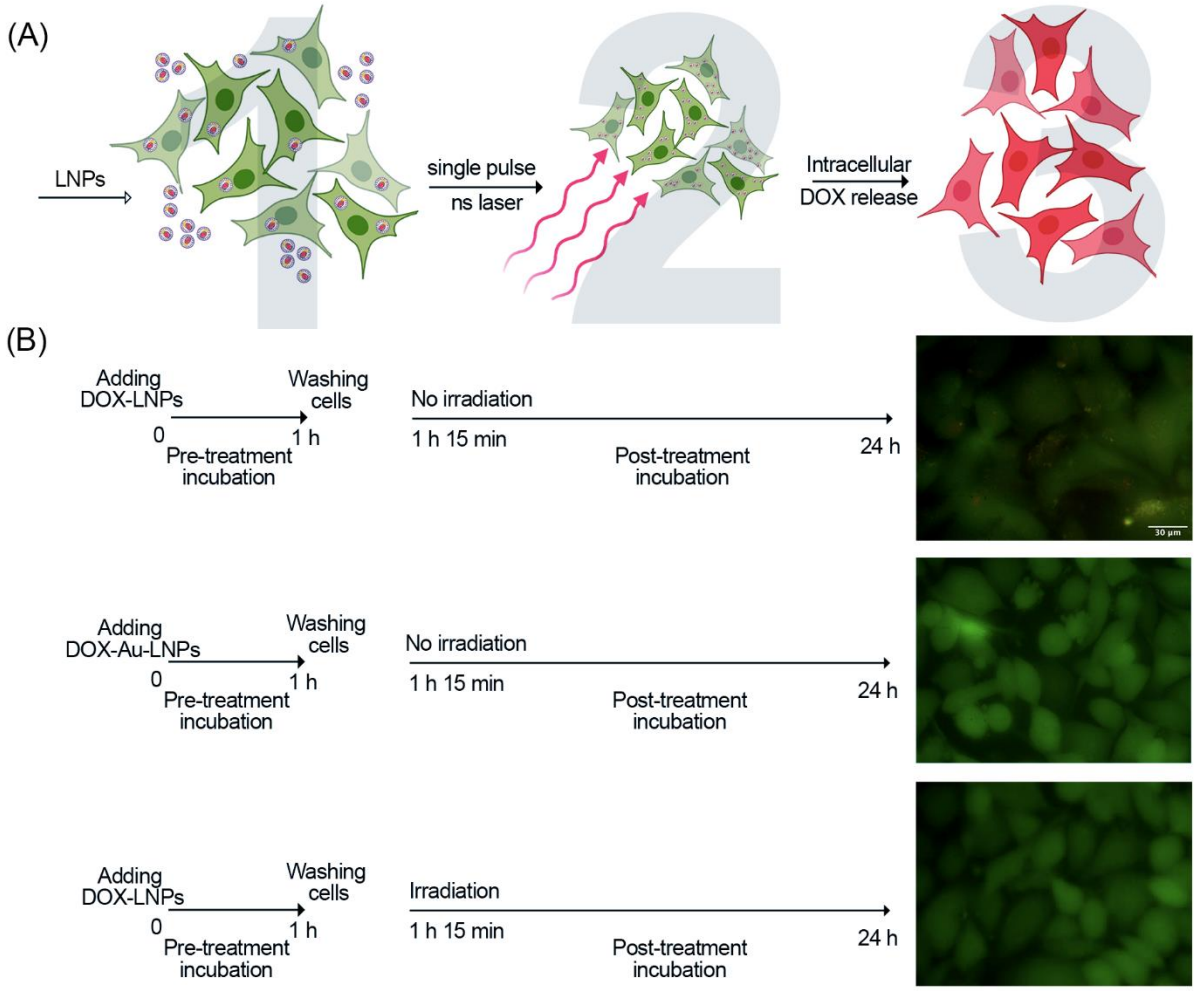

Figure S2. (A) Representative schematic of stimuli-responsive intracellular DOX release following strategy-II (1 h pre-incubation with LNPs). (B) Different control groups of DOX-Au-LNPs (50 µg/mL) and DOX-LNPs (50 µg/mL) with and without the irradiation.

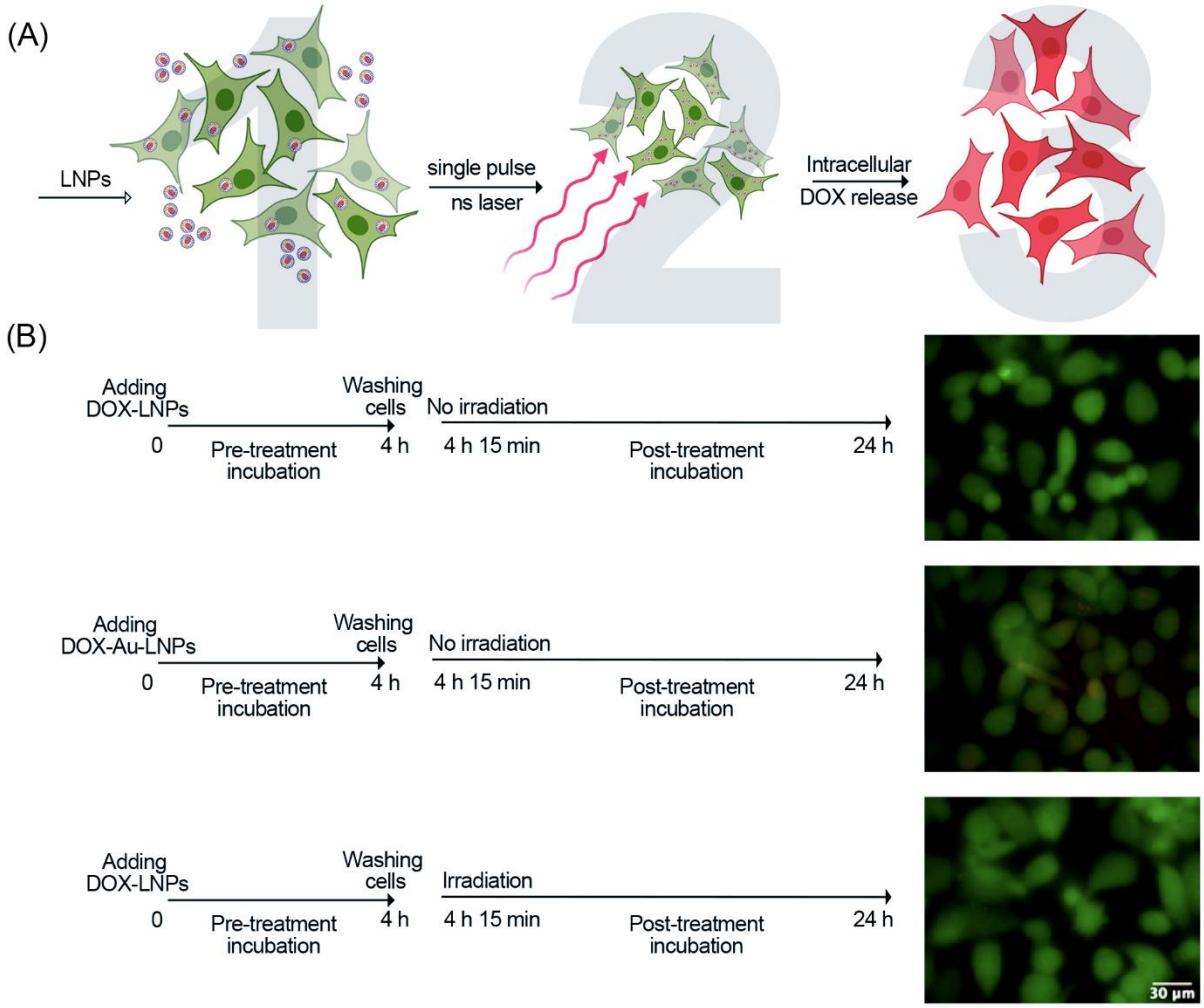

Figure S3. (A) Representative schematic of stimuli-responsive intracellular DOX release following strategy-III (4 h pre-incubation with LNPs). (B) Different control groups of DOX-Au-LNPs (50 µg/mL) and DOX-LNPs (50 µg/mL) with and without the irradiation.

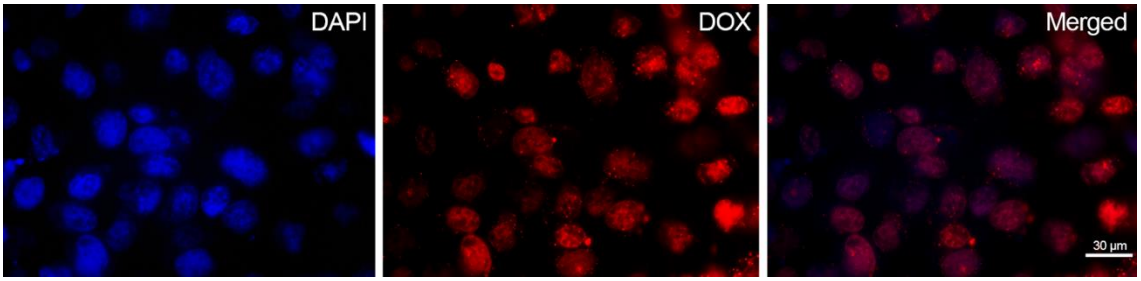

Figure S4. Representative fluorescence micrograph of the nuclear accumulation of DOX.

S.2. Scanning speed

Due to the Gaussian spatial beam profile, there is, conceptually, a trade-off between the sample irradiation coverage at a certain fluence value while ensuring at the same time single pulse exposure. This is related also to the fact that, in the numerical modeling, the attained temperatures

at the peak of the pulse are considered. For instance, at a scanning speed of 200 μm/s, ~ 22% of the sample is exposed to < 80% of the peak laser fluence (see Figure S1). Our choice of 100 and 50 μm/s ensures nonetheless, both high sample coverage and exposure to at least a single pulse of >91% of the peak fluence. The low repetition rate of the laser provides an advantage to this end since each consecutive pulse is launched with a delay of ~100 ms, which is far larger than the thermal relaxation of the sample. As such, each effect caused by a given incident pulse is considered nearly independent in the scanning speed regime of 50-100 μm/s.

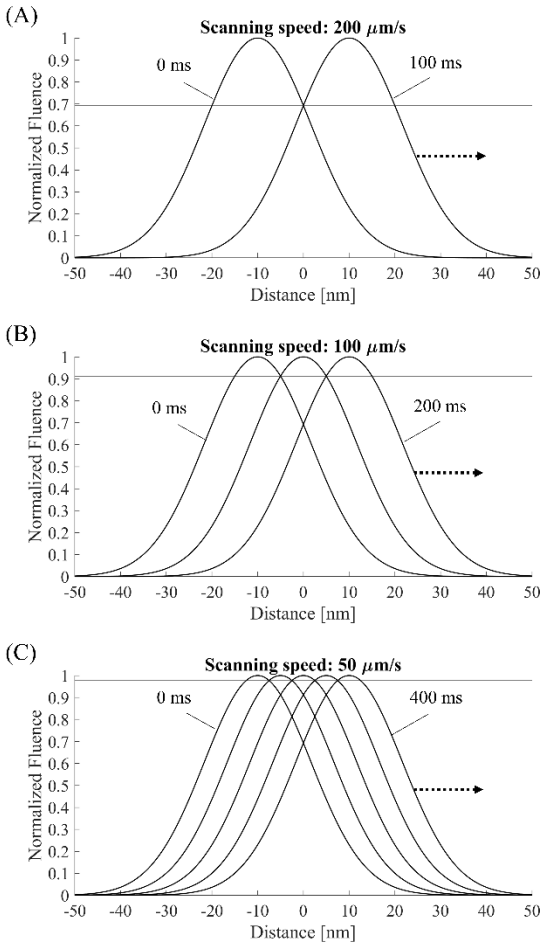

Figure S5. Beam profile sample coverage upon scanning. (A) For a scanning speed of 200 μm/s, a partial overlap of the beam is attained when ~22% of the sample is exposed to less than 80% of the laser peak fluence. (B) By employing a scanning speed of 100 μm/s, the whole sample is exposed to >91% of the peak fluence, whereas (C) for a scanning speed of 50 μm/s, the whole sample is exposed to >98% of the peak fluence. Thus, conceptually there is a trade-off between sample coverage and ensuring single pulse exposure. Nonetheless, the repetition rate of the laser is low (10 Hz), so each consecutive pulse is launched with a delay of ~100 ms, which is far larger than the thermal relaxation time of the sample and each incident pulse is nearly independent.

S.3. Numerical simulations

The two-temperature model (TTM) approximation [1, 2]was followed, assuming that the laser energy is first deposited to the electron gas of the particle and subsequently transferred to its phonon subsystem. A boundary condition was imposed at the interface with the surrounding medium so that a diffusion equation can be coupled to the TTM as:

$$C_e(T_e)\frac{dT_e}{dt} = -G(T_e - T_l) + \frac{\sigma(\omega, T_e, T_l)I(t)}{V_{np}}$$

$$C_l(T_l)\frac{dT_l}{dt} = G(T_e - T_l) - \frac{3g}{R_{np}}\left(T_l - T_m|_{r=R_{np}}\right)$$

$$C_m(T_m)\frac{\partial T_m}{\partial t} = \frac{1}{r^2}\frac{\partial}{\partial r}\left(k_m r^2 \frac{\partial T_m}{\partial r}\right)$$

where the subscripts e, l and m stand for "electron", "lattice" and "medium", respectively, C denotes the heat capacity, G is the electron-phonon coupling, $g \propto C_m k_m$ [3] is the interface (Au-medium) conductance, R_{np} is the radius of the Au particle, k_m the thermal conductivity of the medium (see Table S1) and $I(t)$ the laser pulse intensity, formulated by $I(t) = 2\frac{F}{t_p}\sqrt{\frac{ln2}{\pi}}e^{-4ln2\frac{t^2}{t_p^2}}$ where F is the laser pulse fluence and t_p stands for the FWHM (full width at half maximum) pulsewidth.

The AuNPs absorption cross-section is known to undergo substantial variations as a function of temperature. To model this effect, we first employed the following analytical description of the Au dielectric function [4] $\varepsilon(\omega) = \varepsilon_\infty - \frac{\omega_p^2}{\omega^2 + i\gamma\omega} - \frac{A_{ib}}{2(\omega + i\gamma_{ib})^2}\ln\left(1 - \left(\frac{\omega - \gamma_{ib}}{\omega_{ib}}\right)^2\right)$ (see Table S1). We assigned temperature dependence accounting for modulations due to i) electronic temperature increase and ii) lattice temperature increase [5, 6]. The first typically induces a broadening $\delta\gamma_{e-e}(\omega, T_e) \approx \gamma\frac{2\pi k_B}{\hbar\omega}\left({T_e}^2 - {T_0}^2\right)$ on γ, so that $\delta\varepsilon^e(\omega, T_e) \approx \frac{\omega_p^2}{\omega^3}\delta\gamma_{e-e}(\omega, T_e)\left(\frac{2\gamma}{\omega} + i\right)$ is the corresponding shift of the dielectric function. Lattice temperature results typically on broadening $\delta\gamma_{e-ph}$ so that a shift $\delta\varepsilon^{l,1}(\omega, T_l) \approx i\frac{\omega_p^2}{\omega^2}\frac{\partial\gamma_{e-ph}}{\partial T}\delta T_l$ is estimated, where we have used $\frac{\partial\gamma_{e-ph}}{\partial T} \approx 0.11$ meV/K [5, 6]. In addition, the Au lattice expands affecting the real part of the dielectric function, with a shift $\delta\varepsilon^{l,2}(\omega, T_l) \approx \frac{\omega_p^2}{\omega^2}3a_L\delta T_l$ where we have used the value of linear expansion coefficient of gold $a_L \approx 1.42 \times 10^{-5}$ K^{-1} [5, 6]. Finally, Fermi level smearing following electron thermalization affects interband transitions and induces a shift $\delta\varepsilon^{l,int}(\omega, T_l) = \frac{\partial\varepsilon^{int}}{\partial T}\delta T_l$, where we have used $\frac{\partial\varepsilon^{int}}{\partial T} \approx 2.9 \times 10^{-3}$ K^{-1} [5, 6]. Conclusively, the total shift on the dielectric function reads:

$$\varepsilon(\omega, T_e, T_l) \approx \varepsilon(\omega) + \delta\varepsilon^e(\omega, T_e) + \delta\varepsilon^{l,1}(\omega, T_l) + \delta\varepsilon^{l,2}(\omega, T_l) + \delta\varepsilon^{l,int}(\omega, T_l)$$

Subsequently, we use the quasi-static approximation to estimate the absorption cross section of a single gold nanoparticle according to the relationship

$$\sigma(\omega, T_e, T_l) = \frac{8\pi^2\varepsilon_m^{1/2}}{\lambda}{R_{np}}^3 Im\left\{\frac{\varepsilon(\omega, T_e, T_l) - \varepsilon_0}{\varepsilon(\omega, T_e, T_l) + 2\varepsilon_0}\right\}$$

where ε_m denotes the permittivity of the lipid layer and V_{np} is the volume of the particle.

To account for collective heating effects, the solutions of TTM for the maximum temperature spatial profile around a single nanoparticle were summed spatially for a cluster of particles (varying from 2 to 7 particles) as $\Delta T_{max}^{total}(r) = \sum_1^i \Delta T_{max}^i(r - r_i)$, for the case of the interparticle distance of 1 nm and r in the surrounding medium (lipid or water.

Table S1. Parameters used for numerical simulations.

Parameter	Symbol	Value	Ref.
Au permittivity			
Background contribution to permittivity*	ε_∞	$= 4$	
Fermi velocity	u_F	$= 1.4 \times 10^6\ m\ s^{-1}$	[7]
Bulk plasmon decoherence*	γ_b	$= 1 \times 10^{14}\ s^{-1}$	
Particle plasmon decoherence	γ	$= \gamma_b + u_F/R_{np}$	[8]
Plasma radial frequency	ω_p	$1.37 \times 10^{16}\ rad\ s^{-1}$	
Interband transition threshold radial frequency*	ω_{ib}	$= 3.87 \times 10^{15}\ rad\ s^{-1}$	[7]
Interband transition broadening*	γ_{ib}	$= 3.8 \times 10^{14}\ s^{-1}$	
Interband transition oscillator strength*	A_{ib}	$= 40$	
Linear expansion coefficient	$\partial\gamma_{e-ph}/\partial T$	$= 0.11\ meV\ K^{-1}$	[5, 6]
	a_L	$= 1.42 \times 10^{-5}\ K^{-1}$	[5, 6]
	$\partial\varepsilon^{int}/\partial T$	$= 2.9 \times 10^{-3}\ K^{-1}$	[9]
Au Nanoparticle properties			
Medium permittivity (water)	ε_m	$= 1.77$	
Medium permittivity (lipid)		≈ 2.3	
Au density	ρ_{Au}	$19\ 300\ kg\ m^{-3}$	
Radius of nanoparticle	R_{np}	$2.5\ nm$	
Electron-phonon coupling parameter	G	$2.5 \times 10^{16}\ W\ m^{-3}\ K^{-1}$	[10]
Lattice heat capacity	C_l	$= \rho_{Au}(119 + 3.061 \times 10^{-2} T_l)\ (J\ m^{-3}\ K^{-1})$	[11]
Electron heat capacity	C_e	$70 T_e\ (J\ m^{-3}\ K^{-1})$	[12]
Medium properties			
Medium permittivity (water)	ε_m	$= 1.77$	
Medium permittivity (lipid)		≈ 2.3	[13]
Thermal conductivity**	k_m	$\approx 0.58\ W\ m^{-1}\ K^{-1}$	[14]
Medium density**	ρ_m	$\approx 1000\ kg\ m^{-3}$	[15]
Cholesterol molar heat capacity	$c_{m,ch}$	$\approx 600\ J\ K^{-1} mol^{-1}$	[16]
Molar weight of cholesterol	$M_{m,ch}$	$\approx 387\ g\ mol^{-1}$	[17]
DSPC molar heat capacity	$c_{m,DSPC}$	$\approx 1600\ J\ K^{-1} mol^{-1}$	[15]
Molar weight of DSPC	$M_{m,DSPC}$	$\approx 790\ g\ mol^{-1}$	[17]
Heat capacity (water)	C_m	$= 4.2 \times 10^6\ J\ m^{-3}\ K^{-1}$	[1, 2]
Heat capacity (lipid)		$\approx \rho_m\left(0.4 c_{m,ch}\ {M_{m,ch}}^{-1} + 0.6 c_{m,DSPC}\ {M_{m,DSPC}}^{-1}\right)$ $(J\ m^{-3}\ K^{-1})$	
Interface conductance (water)	g	$= 105$ MW m^{-2} K^{-1}	[18]
Interface conductance (lipid)		≈ 46 MW m^{-2} K^{-1} (Estimated by $g \propto C_m k_m$)	[3]

* Fitting parameters based on data found in [7]

** Considered almost unchanged for both water and lipid medium

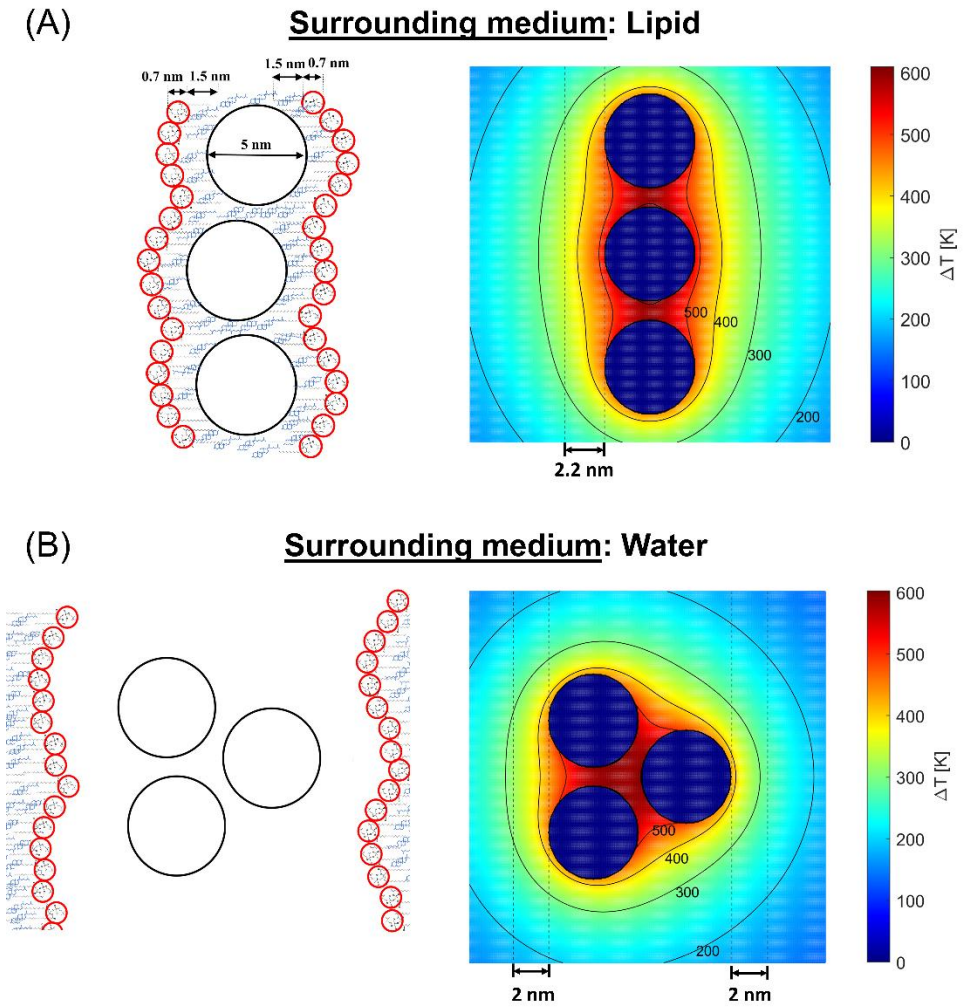

Figure S6. Simulation of the collective heating effect of a cluster (trimer) of AuNPs at a laser fluence of 1.6 J/cm^2. (A) Three AuNPs are located within a lipid bilayer. (B) Three AuNPs reside within an aqueous compartment of an oligollamelar vesicle. Interparticle distance: 1 nm.

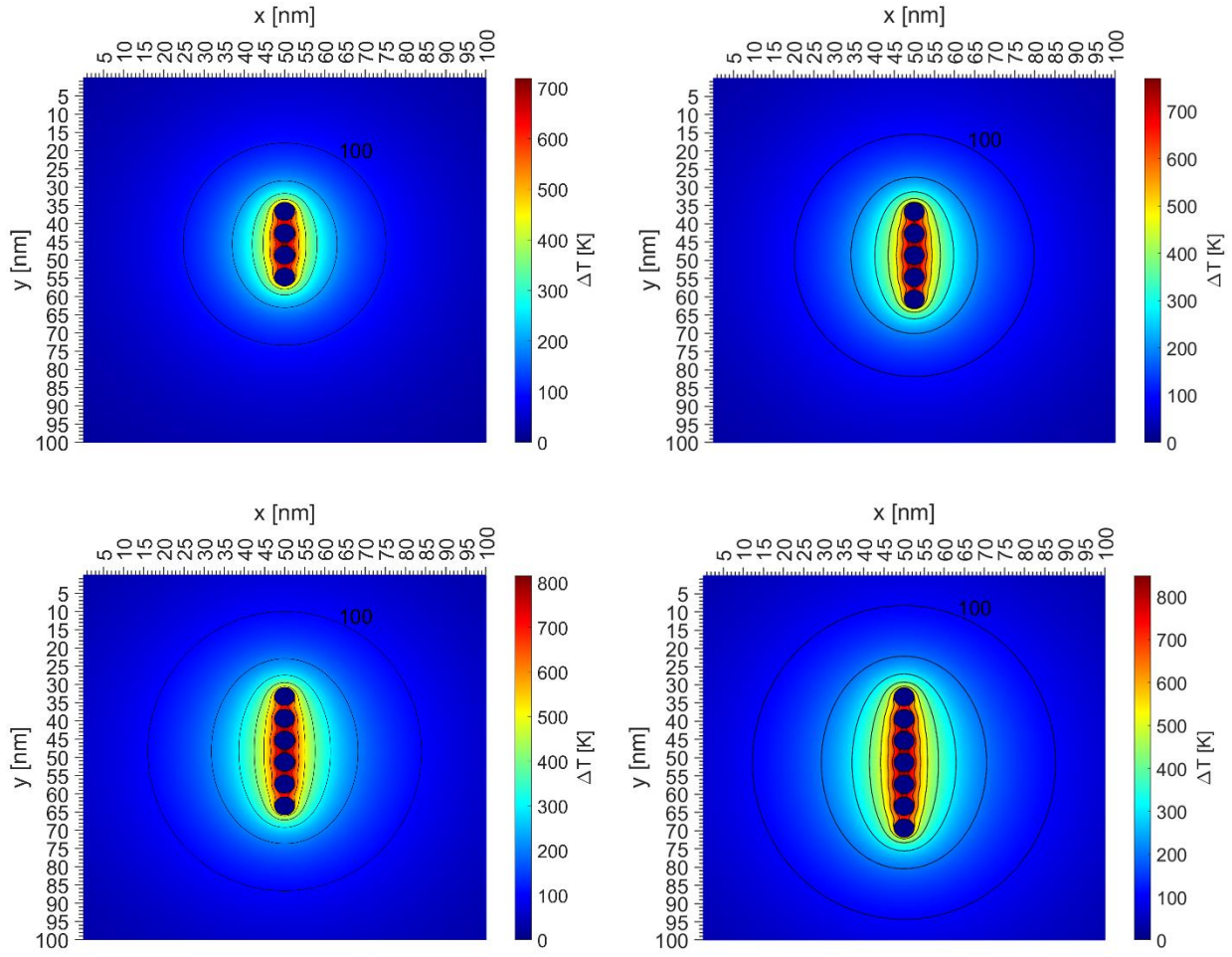

Figure S7. Simulation of the collective heating effect of clusters of AuNPs of increasing number at a laser fluence of 1.6 J/cm^2 at the peak of the pulse. Clusters in line formation are considered with an interparticle distance of 1 nm. The surrounding medium is assumed to be lipid. The isolines of temperature are drawn on each figure with a step of 100 K.

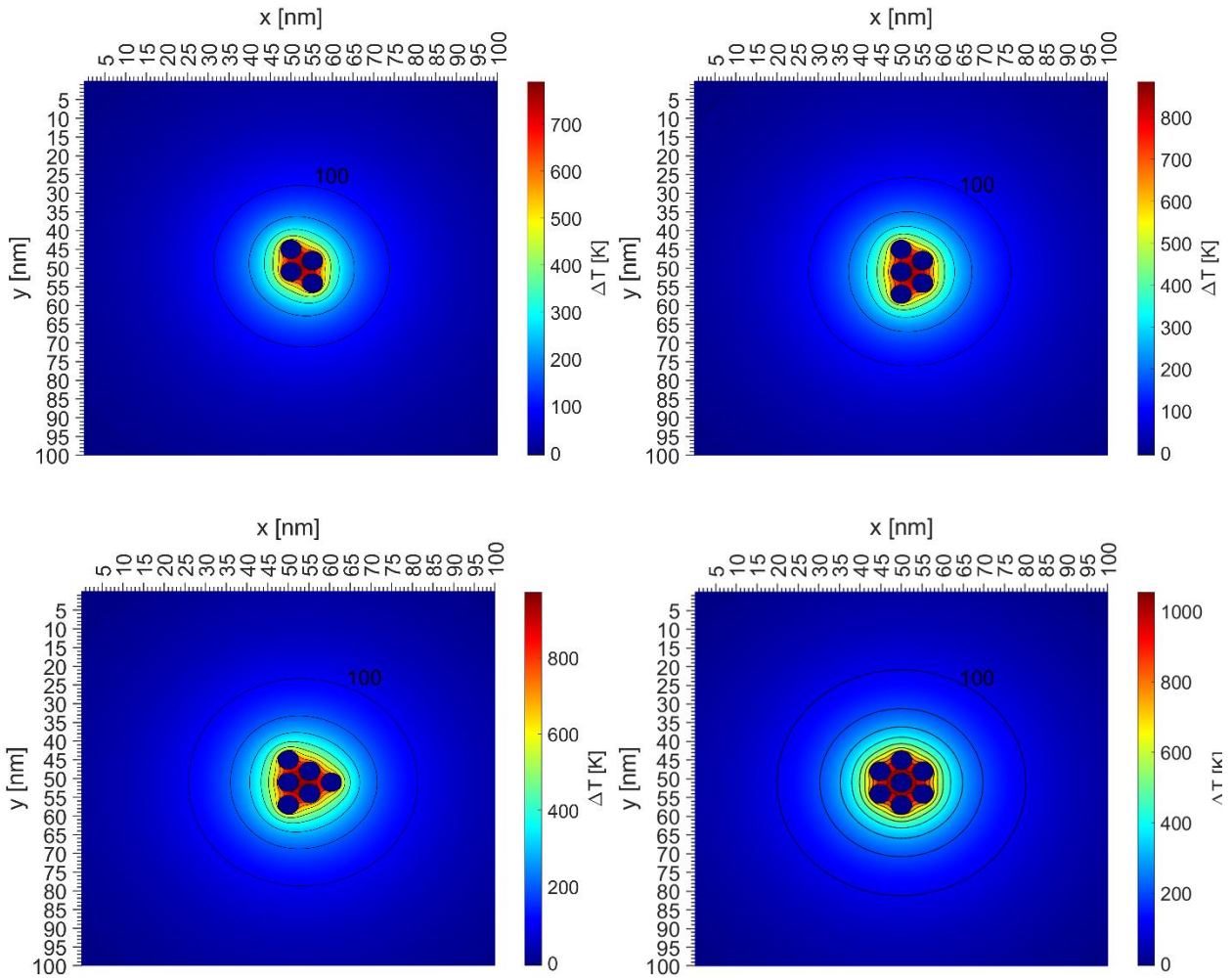

Figure S8. Same as Figure S2, however, a closed-packed cluster is considered, and the particles are assumed to be surrounded by water.

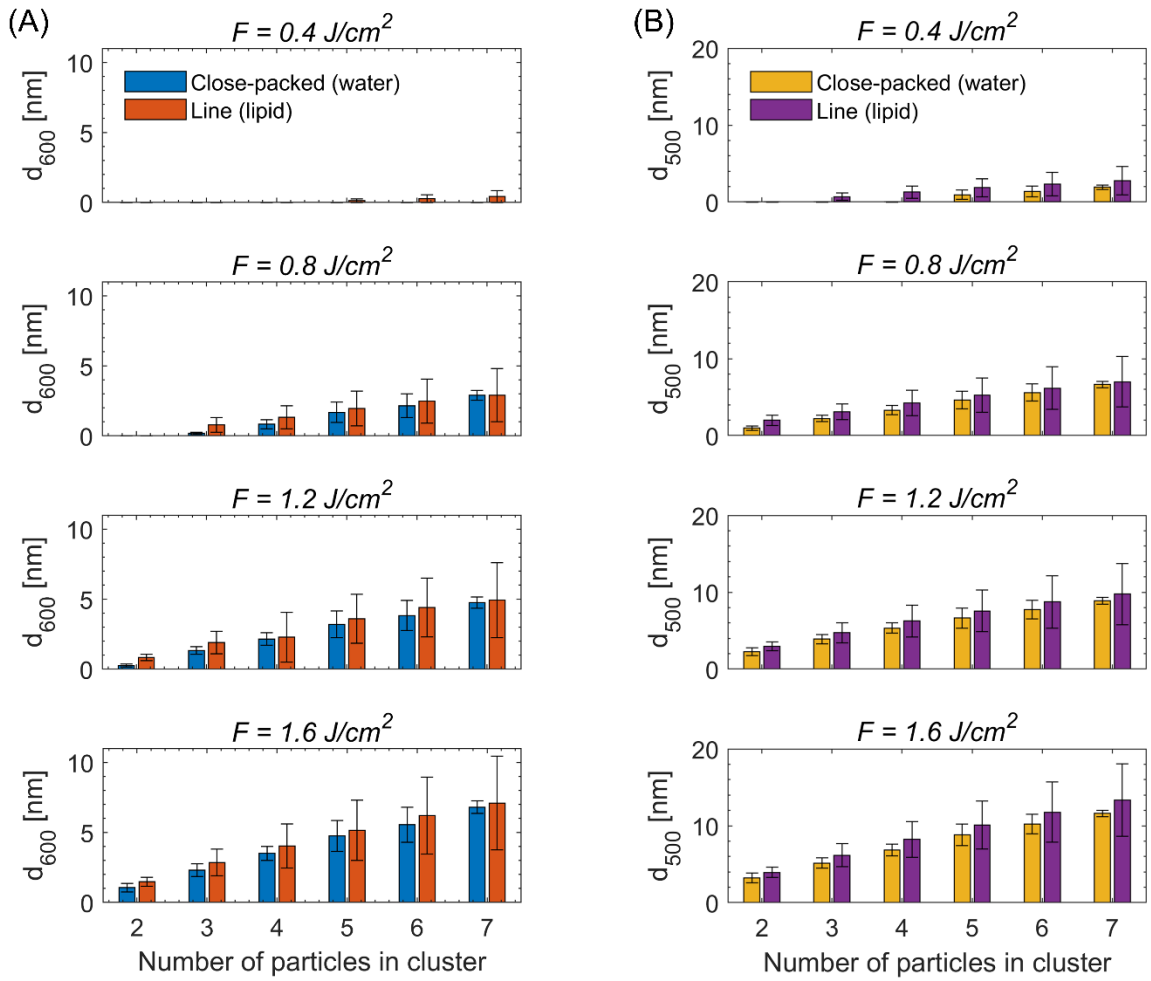

Figure S9. (a) The distance d_{600} (from the perimeter of a cluster) at which 600 K absolute temperature is reached at the peak of the laser pulse, as a function of the number of particles in the cluster. The two distinct cases presented in Figures S1-S3 (line formation in the lipid bilayer and close-packed formation in water) are considered. The temperature of 600 K is associated with the thermal degradation of DSPC/cholesterol/DDAB liposomes (6:4:1 molar ratio) [19]. (b) Same as (a), but for the distance d_{500} at which 500 K absolute temperature is reached at the peak of the laser pulse. The temperature of 500 K is associated with thermal degradation onset of doxorubicin [20].

References

[1] M. Strasser, K. Setoura, U. Langbein, S. Hashimoto, Computational modeling of pulsed laser-induced heating and evaporation of gold nanoparticles, The Journal of Physical Chemistry C 118(44) (2014) 25748-25755.
[2] D. Werner, S. Hashimoto, Improved working model for interpreting the excitation wavelength- and fluence-dependent response in pulsed laser-induced size reduction of aqueous gold nanoparticles, The Journal of Physical Chemistry C 115(12) (2011) 5063-5072.
[3] A. Siems, S.A. Weber, J. Boneberg, A. Plech, Thermodynamics of nanosecond nanobubble formation at laser-excited metal nanoparticles, New Journal of Physics 13(4) (2011) 043018.

[4] D. Rioux, S. Vallières, S. Besner, P. Muñoz, E. Mazur, M. Meunier, An analytic model for the dielectric function of Au, Ag, and their alloys, Advanced Optical Materials 2(2) (2014) 176-182.
[5] T. Stoll, P. Maioli, A. Crut, N. Del Fatti, F. Vallée, Advances in femto-nano-optics: ultrafast nonlinearity of metal nanoparticles, The European Physical Journal B 87 (2014) 1-19.
[6] F. Vallée, N. Del Fatti, Ultrafast nonlinear plasmonics, Plasmonics: Theory and Applications (2013) 167-205.
[7] P.B. Johnson, R.-W. Christy, Optical constants of the noble metals, Physical review B 6(12) (1972) 4370.
[8] U. Kreibig, M. Vollmer, Optical properties of metal clusters (Chapter 2), Springer Science & Business Media2013.
[9] F. Hache, D. Ricard, C. Flytzanis, U. Kreibig, The optical Kerr effect in small metal particles and metal colloids: the case of gold, Applied Physics A 47 (1988) 347-357.
[10] P. Grua, J. Morreeuw, H. Bercegol, G. Jonusauskas, F. Vallée, Electron kinetics and emission for metal nanoparticles exposed to intense laser pulses, Physical Review B 68(3) (2003) 035424.
[11] R. Perry, G. DW, Perry's chemical engineers' handbook, 8th illustrated ed, New York: McGraw-Hill (2007).
[12] J. Hohlfeld, S.-S. Wellershoff, J. Güdde, U. Conrad, V. Jähnke, E. Matthias, Electron and lattice dynamics following optical excitation of metals, Chemical Physics 251(1-3) (2000) 237-258.
[13] Y. Jin, J. Chen, L. Xu, P. Wang, Refractive index measurement for biomaterial samples by total internal reflection, Physics in Medicine & Biology 51(20) (2006) N371.
[14] N. Rafieiolhosseini, M.R. Ejtehadi, Thermal conductivity of the cell membrane in the presence of cholesterol and amyloid precursor protein, Physical Review E 102(4) (2020) 042401.
[15] T. Heimburg, Mechanical aspects of membrane thermodynamics. Estimation of the mechanical properties of lipid membranes close to the chain melting transition from calorimetry, Biochimica et Biophysica Acta (BBA)-Biomembranes 1415(1) (1998) 147-162.
[16] J. Van Miltenburg, A. Van Genderen, G. Van den Berg, Design improvements in adiabatic calorimetry: The heat capacity of cholesterol between 10 and 425 K, Thermochimica Acta 319(1-2) (1998) 151-162.
[17] NCBI, PubChem Compound Summary for (i) CID 94190, 1,2-Distearoyl-sn-glycero-3-phosphocholine for (ii) CID 5997, Cholesterol, 2023.
[18] A. Plech, V. Kotaidis, S. Grésillon, C. Dahmen, G. Von Plessen, Laser-induced heating and melting of gold nanoparticles studied by time-resolved x-ray scattering, Physical Review B 70(19) (2004) 195423.
[19] G. Jose, Y.-J. Lu, H.-A. Chen, H.-L. Hsu, J.-T. Hung, T. Anilkumar, J.-P. Chen, Hyaluronic acid modified bubble-generating magnetic liposomes for targeted delivery of doxorubicin, Journal of Magnetism and Magnetic Materials 474 (2019) 355-364.
[20] B. Manocha, A. Margaritis, Controlled release of doxorubicin from doxorubicin/γ-polyglutamic acid ionic complex, Journal of Nanomaterials 2010 (2010) 1-8.